Natural Fault-Tolerant Control With Minimum Copper Loss in Full Torque Operation Range for Dual Three-Phase PMSM Under Open-Circuit Fault

Qiang Geng, *Member, IEEE*, Zhongchen Li, Huimin Wang, *Member, IEEE*, Guozheng Zhang, *Member, IEEE*, and Zhanqing Zhou, *Member, IEEE*

***Abstract*—Traditional perspective considers that there is a trade-off between the postfault operational performance and the implementation complexity of the control scheme. To approach this problem, this article proposes a natural full range minimum-loss strategy by analyzing the current relation between torque subspace and harmonic subspace. The harmonic subspace current references satisfying full range minimum-loss are generated by a simple expression according to the real-time subspace current vector features. Compared with existing fault-tolerant control methods, the proposed strategy does not need complicate fault diagnosis, as well as offline or online optimization process. The experimental results demonstrate that the proposed fault-tolerant control strategy can achieve smooth prefault to postfault transition and FRML simultaneously.**

***Index Terms*—Dual three-phase permanent magnet synchronous motor (DTP-PMSM), full range minimum-loss (FRML), natural fault-tolerant control, open-circuit fault (OCF).**

NOMENCLATURE

Acronyms

DTP-PMSM	Dual three-phase permanent magnet synchronous motor.
OCF	Open-circuit fault.
OSF	Open-switch fault.
MMF	Magnetomotive force.
VSD	Vector space decomposition.
ML	Minimum copper loss.
MT	Maximum torque.
FRML	Full range minimum copper loss.
TOR	Torque operation range.
NFRML	Natural full range minimum-loss.
QPR	Quasi-proportional-resonant.

Variables

i_x	Phase currents of the dual three-phase PMSM (x = A, B, C, D, E, F).
$I_{\mathrm{m}x}$	Amplitude of phase current (x = A, B, C, D, E, F).
ω_{e}	Rotor electrical angular speed.
ω_{m}	Rotor mechanical angular speed.
φ_x	Initial phase of phase currents (x = A, B, C, D, E, F).
φ_{xy}	Phase of x–y subspace current vector when the α-β subspace current vector lies on the faulty phase axis.
i_α, i_β	α- and β-axes current in the VSD model.
$i_{\mathrm{x}}, i_{\mathrm{y}}$	x- and y-axes current in the VSD model.
I_{rt}	Rated phase current.
$i_\alpha^{\mathrm{rt}}, i_\beta^{\mathrm{rt}}$	Rated current of α- and β-axes current.
$\lvert\boldsymbol{i}_{\alpha\beta}\rvert$	Amplitude of the α-β subspace current vector.
$I_{\mathrm{lim}}^{\mathrm{ML}}$	Maximum amplitude of $\lvert\boldsymbol{i}_{\alpha\beta}\rvert$ that can be generated in the ML mode.
$I_{\mathrm{lim}}^{\mathrm{MT}}$	Maximum amplitude of $\lvert\boldsymbol{i}_{\alpha\beta}\rvert$ that can be generated in the MT mode.
$A_{\mathrm{ML}}, A_{\mathrm{MT}}, A_{\mathrm{FRML}}$	Amplitude of phase current in ML, MT, and FRML strategy, respectively.
P_{Cu}^*	Normalized copper loss.
θ_{f}	Phase of harmonic current vector in the fault phase harmonic coordinate system.

Manuscript received 18 April 2023; revised 26 July 2023 and 11 September 2023; accepted 29 September 2023. Date of publication 10 October 2023; date of current version 6 December 2023. This work was supported in part by the National Natural Science Foundation of China under Grants 52077154, 52377066, and 52277064. Recommended for publication by Associate Editor A. M. Trzynadlowski. *(Corresponding author: Zhanqing Zhou.)*

Qiang Geng, Huimin Wang, Guozheng Zhang, and Zhanqing Zhou are with the School of Electrical Engineering, Tiangong University, Tianjin 300387, China (e-mail: gengqiang@tju.edu.cn; wanghuimin@tiangong.edu.cn; zhanggz@tju.edu.cn; zhouzhanqing@tiangong.edu.cn).

Zhongchen Li is with the School of Electronics and Information Engineering, Tiangong University, Tianjin 300387, China (e-mail: lizhongchen@tiangong.edu.cn).

Color versions of one or more figures in this article are available at https://doi.org/10.1109/TPEL.2023.3323570.

Digital Object Identifier 10.1109/TPEL.2023.3323570

I. INTRODUCTION

DUE to the better fault-tolerant capability than traditional three-phase motor, multiphase motors have been used in safety-critical applications, such as aerospace, offshore wind generator, and ship propulsion [1], [2], [3]. Among the different types of multiphase motors, DTP-PMSM drives have received significant attention since it can take full advantages of well-built three-phase PMSM drives [4].

The main electrical faults in motor drives are single-phase OCF and power switch OSF, which can cause serious torque pulsations, mechanical vibrations, and even lead to breakdown

of the drive system. The analysis presented in [5] shows that it will achieve the prefault torque output under OCF as long as the rotating MMF is maintained the same as the prefault operation. This can be achieved in different ways in DTP-PMSM drives without extra hardware.

The first way is called as redundant control strategy. In the postfault operation, the whole three-phase winding containing the open-circuit phase is disabled and isolated [6]. In this case, the DTP-PMSM is degraded to a conventional three-phase PMSM and the maximum output power/torque will be greatly reduced to half of the normal operation.

The second approach is based on software reconfiguration. Specifically, these approaches for the reconfiguration can be divided into two categories: reconstructing the machine model [7], [8] or modifying current references [9], [10], [11], [12], [13], [14], [15], [16], [17], [18], [19], [20]. However, the former methods need the tedious offline modeling process and the complexity of the method ill dramatically increase when there is more than one faulty phase. Therefore, these methods are not widely used even though the theory of VSD has been well established. By comparison, the latter methods have been extensively studied because of the superiorities of easier implementation and adapting various motor types.

The existent fault-tolerant current references optimization methods can be divided into ML strategy [9], [10], MT strategy [11], [12], [13], [14], and FRML strategy [15], [16], [17], [18], [19], [20]. The ML strategy, aiming to minimize the stator copper losses, can achieve more efficient operation. However, heterogeneous phase currents in the ML operation constrain the TOR. The MT strategy aims at the widest TOR while ensuring that all the healthy phase current amplitudes are below the rated value. However, this strategy has higher copper loss than the ML strategy. FRML strategy aims to obtain the ML for each torque reference in the whole TOR (same as the TOR of MT strategy in the same fault condition).

The majority of the abovementioned methods add the restrictions of sinusoidal current patterns in the process of optimizing the current, which simplifies the algorithm and implementation complexity. However, it is impossible to fully release the performance of the faulty machine due to the additional constrains. By comparison, the schemes with partially or completely unconstrained current patterns can improve the torque output capability and reduce copper loss to a certain extent [10], [11], [12]. However, the lack of constraints and nonsinusoidal current patterns will pose obstacles to current optimization, controller design, and tuning. Therefore, to some extent, FRML strategy is the most convenient and has attracted more and more attention in the past decade.

The current references of FRML are normally obtained offline and stored in lookup table [16], [17]. However, this method has the same drawbacks as reconstructing the machine model, i.e., occupying substantial storage space if the machine phase number is high. Moreover, searching process will consume extra time. The online FRML strategies proposed in [18] and [19] are based on an online iterative algorithm for calculating the optimal current references. Although the storage cost of this method is small, it leads to a large computational burden. A different perspective for achieving FRML is proposed in [15], which regard FRML as the result of the interaction of ML and MT with a certain proportion. However, a specific solution is not given in this article. In [20], an approximate FRML strategy that directly calculates the current references through a closed-form expression is proposed. Although this method still needs to store the reference current coefficients of ML and MT strategies for different OCF cases, and the copper loss is slightly higher than that with the traditional FRML schemes, it significantly eases the implement complexity.

It should be emphasized that fault detection and location are required for realizing the abovementioned fault-tolerant control strategies, i.e., reliable fault diagnosis results are the premise of the effective fault tolerant control. As an alternative to the abovementioned fault-tolerant control methods, natural (also known as passive or diagnosis-free self-healing) fault-tolerant control scheme are reported in [21], [22], [23], [24], [25], [26], [27], and [28]. These methods can be regarded as a universal control scheme that can achieve almost the same performance as prefault operation without fault diagnosis and location process. As stated in [21], the main cause of flux/torque disturbances under the fault situation is the conflict goal between the torque subspace and the harmonic subspace controllers. Therefore, the existing passive fault-tolerant control scheme can be divided into three categories. The first category is fulfilled by disabling the harmonic subspace control [21], [22], [23], [24]. The second category avoids the control conflict between controllers by cascading harmonic subspace controller with a notch filter with specially designed cutoff frequency [25], [26]. The basic idea of the last category is to modify the subspace controller references to maintain the constant MMF [27], [28]. However, the existent passive fault-tolerant control cannot achieve FRML since these methods are not able to actively regulate the harmonic subspace currents [22].

To the best of the authors' knowledge, there is no fault-tolerant control scheme that has the merits of both natural fault-tolerant control and FRML scheme. In other words, the existent fault-tolerant control scheme is hard to achieve high performance and low algorithm complexity simultaneously. This article aims to fill this gap and presents a NFRML strategy for OCF of DTP-PMSM drives. The main work of this article is focused on the following parts. First, the current features of ML, MT, and FRML strategies are qualitatively and quantitatively analyzed respectively. Second, NFRML control scheme is designed based on the features of current vector trajectory. Finally, the validity of the proposed scheme is experimentally verified under OCF of DTP-PMSM drive.

II. Background

A. Modeling of DTP-PMSM

Fig. 1 shows the stator winding topology of the DTP-PMSM, which has two sets of three-phase stator windings spatially shifted by 30 electrical degrees with isolated neutral points. The two most widely used models for describing the operation of a DTP-PMSM are double-dq model and VSD model [29].

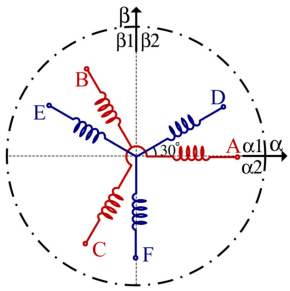

Fig. 1. Stator winding topology of DTP-PMSM.

The double-dq model treats each set of three-phase winding as an independent unit and transforms the machine variables (voltage, current, or flux) into two stationary reference coordinates ($\alpha1$-$\beta1$ and $\alpha2$-$\beta2$) using the following Clarke transformation:

$$\begin{bmatrix} f_{\alpha1} \\ f_{\beta1} \\ f_{\alpha2} \\ f_{\beta2} \end{bmatrix} = \frac{1}{6} \begin{bmatrix} 2 & -1 & -1 & 0 & 0 & 0 \\ 0 & \sqrt{3} & -\sqrt{3} & 0 & 0 & 0 \\ 0 & 0 & 0 & \sqrt{3} & -\sqrt{3} & 0 \\ 0 & 0 & 0 & 1 & 1 & -2 \end{bmatrix} \begin{bmatrix} f_{\mathrm{A}} \\ f_{\mathrm{B}} \\ f_{\mathrm{C}} \\ f_{\mathrm{D}} \\ f_{\mathrm{E}} \\ f_{\mathrm{F}} \end{bmatrix} \tag{1}$$

where symbol f denotes machine variables.

Although the double-dq model provides a clear insight into the physical model of the machine, there is mutual coupling between the two set windings that may affect the stability of control [29].

In the VSD model, the machine variables are mapped into three orthogonal subspaces, i.e., torque subspace, harmonic subspace, and zero-sequence subspace (denoted as α-β, x–y, and o1–o2, respectively):

$$\begin{bmatrix} f_{\alpha} \\ f_{\beta} \\ f_{\mathrm{x}} \\ f_{\mathrm{y}} \\ f_{\mathrm{o1}} \\ f_{\mathrm{o2}} \end{bmatrix} = \frac{1}{6} \begin{bmatrix} 2 & -1 & -1 & \sqrt{3} & -\sqrt{3} & 0 \\ 0 & \sqrt{3} & -\sqrt{3} & 1 & 1 & -2 \\ 2 & -1 & -1 & -\sqrt{3} & \sqrt{3} & 0 \\ 0 & -\sqrt{3} & \sqrt{3} & 1 & 1 & -2 \\ 2 & 2 & 2 & 0 & 0 & 0 \\ 0 & 0 & 0 & 2 & 2 & 2 \end{bmatrix} \begin{bmatrix} f_{\mathrm{A}} \\ f_{\mathrm{B}} \\ f_{\mathrm{C}} \\ f_{\mathrm{D}} \\ f_{\mathrm{E}} \\ f_{\mathrm{F}} \end{bmatrix}. \tag{2}$$

The components in the α-β subspace participate in the electromechanical energy conversion, whereas the x–y and o1–o2 subspaces components only lead to higher copper loss. It should be noted that the o1–o2 subspace can be ignored since there is no zero-sequence current in the DTP-PMSM with isolated neutral points.

Despite the VSD model facilitates the decoupling control of the torque and harmonic components of the machine, it is abstract and hard to interpret with physical variables. The relation between the double-dq model and the VSD model can be obtained from (1) and (2) as

$$\begin{bmatrix} f_{\alpha} \\ f_{\beta} \\ f_{\mathrm{x}} \\ f_{\mathrm{y}} \end{bmatrix} = \begin{bmatrix} 1 & 0 & 1 & 0 \\ 0 & 1 & 0 & 1 \\ 1 & 0 & -1 & 0 \\ 0 & -1 & 0 & 1 \end{bmatrix} \begin{bmatrix} f_{\alpha1} \\ f_{\beta1} \\ f_{\alpha2} \\ f_{\beta2} \end{bmatrix}. \tag{3}$$

It is shown that the α-β components are generated by the two sets of three-phase winding and the x–y components are caused by the asymmetry of the drive. Equation (3), therefore, helps to interpret the VSD model to some extent.

The voltage equations in d–q and x–y subspaces are

$$\begin{cases} u_{\mathrm{d}} = R_{\mathrm{s}} i_{\mathrm{d}} + L_{\mathrm{d}} \frac{\mathrm{d}i_{\mathrm{d}}}{\mathrm{d}t} - \omega_{\mathrm{e}} L_{\mathrm{q}} i_{\mathrm{q}} \\ u_{\mathrm{q}} = R_{\mathrm{s}} i_{\mathrm{q}} + L_{\mathrm{q}} \frac{\mathrm{d}i_{\mathrm{q}}}{\mathrm{d}t} + \omega_{\mathrm{e}} L_{\mathrm{d}} i_{\mathrm{d}} + \omega_{\mathrm{e}} \psi_{\mathrm{f}} \\ u_{\mathrm{x}} = R_{\mathrm{s}} i_{\mathrm{x}} + L_{\mathrm{z}} \frac{\mathrm{d}i_{\mathrm{x}}}{\mathrm{d}t} \\ u_{\mathrm{y}} = R_{\mathrm{s}} i_{\mathrm{y}} + L_{\mathrm{z}} \frac{\mathrm{d}i_{\mathrm{y}}}{\mathrm{d}t} \end{cases} \tag{4}$$

where u_{d}, u_{q}, u_{x}, and u_{y} refer to the stator voltages in d–q and x–y subspace. i_{d}, i_{q}, i_{x}, and $\mathrm{i_y}$ refer to the stator currents in d–q and x–y subspace. L_{d}, L_{q}, and L_{z} refer to stator inductance in d–q and x–y subspaces, respectively. R_{s} denotes the stator resistance, ω_{e} is the rotor electrical angular speed, and ψ_{f} represents the permanent magnet flux.

The electromagnetic torque can be expressed as

$$T_{\mathrm{e}} = 3p \left[\psi_{\mathrm{f}} i_{\mathrm{q}} + \left(L_{\mathrm{d}} - L_{\mathrm{q}} \right) i_{\mathrm{d}} i_{\mathrm{q}} \right] \tag{5}$$

where p denotes the number pole pairs.

The mechanical motion equation can be expressed as

$$J \frac{\mathrm{d}\omega_{\mathrm{m}}}{\mathrm{d}t} = T_{\mathrm{e}} - T_{\mathrm{L}} - B\omega_{\mathrm{m}} \tag{6}$$

where J is the moment of inertia, B represents the friction coefficient, and T_{L} denotes the load torque.

B. Review of the FRML for Single Phase OCF

Thanks to the advantage of multiple degrees of freedom, a number of current references that enable the DTP-PMSM to achieve the expected postfault operation performance. The most convenient approach, as the previous mentioned, is to use the FRML strategy to generate a postfault current references.

For a DTP-PMSM with isolated neutrals, the current constraints under a single-phase OCF can be expressed as

$$\begin{cases} i_{\mathrm{A}} + i_{\mathrm{B}} + i_{\mathrm{C}} = 0, i_{\mathrm{D}} + i_{\mathrm{E}} + i_{\mathrm{F}} = 0 \\ \max \left\{ i_{\mathrm{A}}, i_{\mathrm{B}}, i_{\mathrm{C}}, i_{\mathrm{D}}, i_{\mathrm{E}}, i_{\mathrm{F}} \right\} \le I_{\mathrm{rt}} \\ i_{fp} = 0 \end{cases} \tag{7}$$

where i_{fp} is current of the faulty phase and I_{rt} is the rated phase current amplitude.

Since the α-β currents participate in the electromechanical energy conversion, it is necessary to remain α-β subspace current references unchanged and modify the x–y subspace current references according to the α-β currents, which can be expressed as

$$\begin{bmatrix} i_{\alpha} & i_{\beta} & i_{\mathrm{x}} & i_{\mathrm{y}} \end{bmatrix}^{\mathrm{T}} = \begin{bmatrix} 1 & 0 & k_{\mathrm{x}\alpha} & k_{\mathrm{y}\alpha} \\ 0 & 1 & k_{\mathrm{x}\beta} & k_{\mathrm{y}\beta} \end{bmatrix}^{\mathrm{T}} \begin{bmatrix} i_{\alpha} \\ i_{\beta} \end{bmatrix}. \tag{8}$$

The elements $k_{\mathrm{x}\alpha}$, $k_{\mathrm{y}\alpha}$, $k_{\mathrm{x}\beta}$, and $k_{\mathrm{y}\beta}$ for FRML are obtained by combining (4) and minimizing the normalized copper loss

$$P_{\mathrm{Cu}}^{*} = \frac{i_{\alpha}^2 + i_{\beta}^2 + i_{\mathrm{x}}^2 + i_{\mathrm{y}}^2}{\left(i_{\alpha}^{\mathrm{rt}} \right)^2 + \left(i_{\beta}^{\mathrm{rt}} \right)^2}. \tag{9}$$

TABLE I
AMPLITUDES AND PHASES OF CURRENTS IN ML MODE

ML Mode		Amplitude/Phase					
		I_{mA}/φ_A	I_{mB}/φ_B	I_{mC}/φ_C	I_{mD}/φ_D	I_{mE}/φ_E	I_{mF}/φ_F
Fault Phase	A	0 / ×	M_1 / –π/2	M_1 / π/2	M_2 / 0.089π	M_2 / –0.911π	M_3 / π/2
	B	M_1 / –π/6	0 / ×	M_1 / 5π/6	M_3 / –π/6	M_2 / –0.756π	M_2 / 1.578π
	C	M_1 / π/6	M_1 / –5π/6	0 / ×	M_2 / –0.244π	M_3 / –5π/6	M_2 / –1.422π
	D	M_2 / –0.087π	M_3 / –2π/3	M_2 / –1.256π	0 / ×	M_1 / –2π/3	M_1 / π/3
	E	M_2 / –1.922π	M_2 / –0.744π	M_3 / 2π/3	M_1 / –π/3	0 / ×	M_1 / 2π/3
	F	M_3 / 0	M_2 / –0.589π	M_2 / 0.589π	M_1 / 0	M_1 / π	0 / ×

$M_1 = \sqrt{3}/2 I_m$, $M_2 = \sqrt{13}/2 I_m$, $M_3 = I_m$, and "×" means null.

TABLE II
AMPLITUDES AND PHASES OF CURRENTS IN MT MODE

MT Mode		Amplitude/Phase					
		I_{mA}/φ_A	I_{mB}/φ_B	I_{mC}/φ_C	I_{mD}/φ_D	I_{mE}/φ_E	I_{mF}/φ_F
Fault Phase	A	0 / ×	M / –π/2	M / π/2	M / 0	M / –π	0 / ×
	B	M / –π/6	0 / ×	M / 5π/6	0 / ×	M / –2π/3	M / π/3
	C	M / π/6	M / –5π/6	0 / ×	M / – π/3	0 / ×	M / 2π/3
	D	M / –π/6	0 / ×	M / 5π/6	0 / ×	M / –2π/3	M / π/3
	E	M / π/6	M / –5π/6	0 / ×	M / – π/3	0 / ×	M / 2π/3
	F	0 / ×	M / –π/2	M / π/2	M / 0	M / –π	0 / ×

$M = \sqrt{3}\, I_m$ and "×" means null.

According to the previous studies in [15] and [20], FRML strategy, from a different perspective, can be regard as a tradeoff between ML and MT, and classified into three modes, which are ML mode, MT mode, and hybrid ML and MT mode (abbreviation hybrid mode), respectively. Furthermore, the total α-β current vector $\boldsymbol{i}_{\alpha\beta}$ can be divided into $\boldsymbol{i}_{\alpha\beta\_\mathrm{ML}}$ and $\boldsymbol{i}_{\alpha\beta\_\mathrm{MT}}$. In the ML and MT mode, $\boldsymbol{i}_{\alpha\beta}$ is consistent with $\boldsymbol{i}_{\alpha\beta\_\mathrm{ML}}$ and $\boldsymbol{i}_{\alpha\beta\_\mathrm{MT}}$, respectively, and the amplitude and the phase of the currents are given in Tables I and II. It is notable that the currents of the remaining healthy phases, in the ML mode, show heterogeneous feature, and the largest amplitude is $\sqrt{13}|\boldsymbol{i}_{\alpha\beta}|/2$ (see Table I). On the contrary, in the MT mode, one of the healthy phases has null current, and the rest of healthy phase currents have the same amplitude ($\sqrt{3}|\boldsymbol{i}_{\alpha\beta}|$). Besides, the phase with null current and the faulty phase are orthogonal in the space (see Table II and Fig. 1).

The ratio k of $|\boldsymbol{i}_{\alpha\beta_\mathrm{MT}}|to|\boldsymbol{i}_{\alpha\beta}|$ in the hybrid mode presented in [20] is

$$k = \frac{|\boldsymbol{i}_{\alpha\beta}| - \mathrm{I}_{\mathrm{lim}}^{\mathrm{ML}}}{\mathrm{I}_{\mathrm{lim}}^{\mathrm{MT}} - \mathrm{I}_{\mathrm{lim}}^{\mathrm{ML}}} \tag{10}$$

where $\mathrm{I}_{\mathrm{lim}}^{\mathrm{ML}}$ and $\mathrm{I}_{\mathrm{lim}}^{\mathrm{MT}}$ are the maximum $|\boldsymbol{i}_{\alpha\beta}|$ that can be generated in the ML mode and MT mode, and equal $0.5547 I_{\mathrm{rt}}$ and $0.5773 I_{\mathrm{rt}}$, respectively. Equation (7) can be treated as an approximate formula for calculating the current references of FRML.

III. NATURAL FRML FAULT-TOLERANT CONTROL SCHEME

From previous studies, it is known that both the passive fault-tolerant control and FRML can be realized by modifying the x–y subspace current references. Therefore, the passive fault-tolerant control and the FRML can be implemented simultaneously. For this purpose, a natural fault-tolerant control with FRML scheme is proposed by analyzing the current trajectories in the different modes of FRML and the optimal ratio of the MT to ML modes for FRML.

A. Analysis of Current Vector Trajectories

Assuming without lack of generality that phase A is open circuit. In this section, the current vector trajectories in the α-β and x–y subspaces are analyzed under different conditions.

Equation (3) can be rewritten as the following complex vector form:

$$\begin{cases} \boldsymbol{i}_{\alpha\beta} = 0.5\,(\boldsymbol{i}_{\alpha\beta1} + \boldsymbol{i}_{\alpha\beta2}) \\ \boldsymbol{i}_{\mathrm{xy}} = 0.5(\boldsymbol{i}_{\alpha\beta1} - \boldsymbol{i}_{\alpha\beta2})^* \end{cases} \tag{11}$$

where the superscript "$_*$" denotes the conjugate operation.

According to the symmetric component method, current vectors generated by the two sets of windings in the double-dq coordinate system can be expressed as

$$\begin{cases} \boldsymbol{i}_{\alpha\beta1} = a_1 \boldsymbol{i}_{\alpha\beta+} + a_2 \boldsymbol{i}_{\alpha\beta-} \\ \qquad\quad = a_1\,|\boldsymbol{i}_{\alpha\beta}|\, e^{j\omega_e t} + a_2\,|\boldsymbol{i}_{\alpha\beta}|\, e^{-j\omega_e t} \\ \boldsymbol{i}_{\alpha\beta2} = a_3 \boldsymbol{i}_{\alpha\beta+} + a_4 \boldsymbol{i}_{\alpha\beta-} \\ \qquad\quad = a_3\,|\boldsymbol{i}_{\alpha\beta}|\, e^{j\omega_e t} + a_4\,|\boldsymbol{i}_{\alpha\beta}|\, e^{-j\omega_e t}. \end{cases} \tag{12}$$

Assuming all the normal phase currents with sinusoidal pattern both in normal and fault conditions. There is only positive sequence component in the normal conditions. The coefficients a_1, a_2, a_3, and a_4 in (9) are 0.5, 0, 0.5 and 0, respectively, which means that each set windings contributes half of the electromagnetic torque and the x–y subspace currents is zero.

Due to the OCF, there is an imbalance to the machine, and the current vectors will contain negative sequence component. According to the Kirchhoff's current law, the phase A current is always zero in the postfault situation, and $i_b + i_c = 0$ is satisfied. In other words, the first set of windings can only generate current vectors in the direction of the $\beta 1$-axis, as shown in Fig. 2(a). In order to keep the same MMF in the air gap, the current $i_{\alpha 2}$ needs to compensate the missing $i_{\alpha 1}$. Thus, the

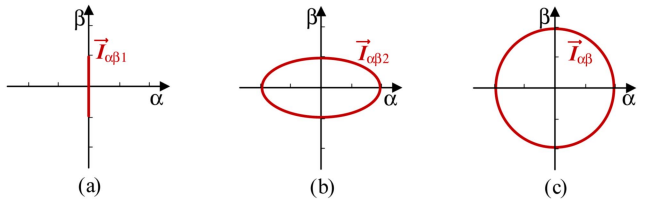

Fig. 2. Current trajectories under phase-A OCF. (a) α_1-β_1 current vector trajectory. (b) α_2-β_2 current vector trajectory. (c) α-β current vector trajectory.

ideal current trajectory will be an ellipse on the α-β plane, as shown in Fig. 2(b). In this condition, the overall current vector trajectory remains unchanged, as shown in Fig. 2(c), and the current vectors generated by the two sets of windings in the double-dq coordinate system can be expressed as

$$\begin{cases} \boldsymbol{i}_{\alpha\beta1} = 0.5\,|\boldsymbol{i}_{\alpha\beta}|\,j\,\sin(\omega_e t) \\ \qquad = 0.25\,|\boldsymbol{i}_{\alpha\beta}|\,e^{j\omega_e t} - 0.25\,|\boldsymbol{i}_{\alpha\beta}|\,e^{-j\omega_e t} \\ \boldsymbol{i}_{\alpha\beta2} = |\boldsymbol{i}_{\alpha\beta}|\cos(\omega_e t) + 0.5\,|\boldsymbol{i}_{\alpha\beta}|\,j\,\sin(\omega_e t) \\ \qquad = 0.75\,|\boldsymbol{i}_{\alpha\beta}|\,e^{j\omega_e t} + 0.25\,|\boldsymbol{i}_{\alpha\beta}|\,e^{-j\omega_e t}. \end{cases} \tag{13}$$

For the VSD model, the α-β and the x–y subspace current vectors, under the same condition, can be deduced from (8) and (10)

$$\begin{cases} \boldsymbol{i}_{\alpha\beta} = |\boldsymbol{i}_{\alpha\beta}|\,e^{j\omega_e t} \\ \boldsymbol{i}_{\mathrm{xy}} = -|\boldsymbol{i}_{\alpha\beta}|\cos(\omega_e t)\,. \end{cases} \tag{14}$$

It can be observed from (11) that the x–y subspace current vector trajectory is a straight line, and its phase is opposite to the α-β current vector if and only if the α-β current vector is located on the A-phase axis. It should also note that the current vector trajectory, in this case, has the same features as in ML mode [30].

From Table II and (8), the x–y subspace current in MT mode can be obtained as

$$\begin{cases} i_x = -i_\alpha \\ i_y = -i_\beta. \end{cases} \tag{15}$$

Following the same procedure, the α-β and x–y subspaces current vectors trajectories in the MT mode can be mathematically expressed as follows:

$$\begin{cases} \boldsymbol{i}_{\alpha\beta} = |\boldsymbol{i}_{\alpha\beta}|\,e^{j\omega_e t} \\ \boldsymbol{i}_{\mathrm{xy}} = |\boldsymbol{i}_{\alpha\beta}|\,e^{j(\omega_e t+\pi)}. \end{cases} \tag{16}$$

It is obvious that the x–y current vector trajectory, in the MT mode, has the same shape as the α-β current vector trajectory, but its phase is opposite to the α-β one.

Based on the previous analysis, it is not hard to imagine that the trajectory of the x–y subspace current vector in the hybrid mode will be an ellipse-like trajectory. The x–y subspace current vector in different modes has the same amplitude and opposite phase as α-β subspace current vector if and only if the α-β current vector lies on the phase A axis. In summary, these specific phase groups are given in Table III, where $\varphi_{\alpha\beta}$ and φ_{xy} are the phases of the α-β and x–y subspace current vectors in the corresponding cases, respectively.

TABLE III
PHASE RELATIONS BETWEEN α-β AND X–Y CURRENT VECTOR TRACES WITH SAME AMPLITUDE AND REVERSE PHASE IN DIFFERENT MODES

Fault phase	φ_{cp}	$(\varphi_{\alpha\beta},\ \varphi_{xy})$
A	0	$(0,\pi)$ or $(\pi,0)$
B	$2\pi/3$	$(2\pi/3,\ \pi/3)$ or $(-\pi/3,\ -2\pi/3)$
C	$-2\pi/3$	$(-2\pi/3,\ -\pi/3)$ or $(\pi/3,\ 2\pi/3)$
D	$\pi/6$	$(\pi/6,\ -\pi/6)$ or $(-5\pi/6,\ 5\pi/6)$
E	$5\pi/6$	$(5\pi/6,\ -5\pi/6)$ or $(-\pi/6,\ \pi/6)$
F	$-\pi/2$	$(-\pi/2,\ \pi/2)$ or $(\pi/2,\ -\pi/2)$

The relation of the current trajectories in different modes and subspaces are summarized as follows.

1) The α-β current vector trajectories in all three FRML strategy modes are circular.
2) The x–y subspace current vector has the same trajectory features in a specific FRML strategy mode.
3) Although the x–y subspace current vector trajectories are different among FRML strategy modes, they have the same amplitude and opposite phase as α-β subspace current vector at a specific phase.

B. Natural Fault-Tolerant Control Strategy in Full TOR

With the aim of fulfilling natural fault-tolerant control in full TOR (the TOR corresponding to $I_{\mathrm{lim}}^{\mathrm{MT}}$), it is necessary to be able to modify the x–y current references according to the amplitude of α-β current vector. The analysis in the former section suggests that this aim is achievable. For this purpose, this subsection proposes a natural fault-tolerant control strategy in the full TOR.

The first step to perform the natural fault-tolerant control is to detect the coupling between the α-β and the x–y currents and determine the coupling relationship between them. According to Table III and Song et al. [26], the coupling relationship between different subspace currents can be expressed as

$$i_{\mathrm{x}}\cos(\varphi_{\mathrm{xy}}) + i_{\mathrm{y}}\sin(\varphi_{\mathrm{xy}}) = i_\alpha\cos(\varphi_{\alpha\beta}) + i_\beta\sin(\varphi_{\alpha\beta}) \tag{17}$$

where φ_{xy} can be calculated by arctan function and x–y currents, and $\varphi_{\alpha\beta}$ can be obtained from Table III according to phase φ_{xy}.

In order to improve robustness against noises in x–y currents, normalized currents should be used in (17). It should be emphasized that although the function of the coupling detection is similar to fault diagnosis algorithm, there are still significant differences between them. The coupling detection is designed based on the fixed current coupling relationships between currents, whereas conventional fault diagnosis algorithms are based on sophisticated signal processing and somewhat subjective as they depend on thresholds selection.

After determining the currents coupling relationship, the x–y currents need to be adjusted accordingly. Considering the x–y current vector trajectories are different for each OCF, a faulty phase harmonic subspace coordinate system shown in Fig. 3 is established to unify the mathematical expression of the x–y current trajectory. The positive direction of the x_f-axis is defined as the direction of x–y current vector when the α-β current vector coincides with the positive direction of the fault phase winding

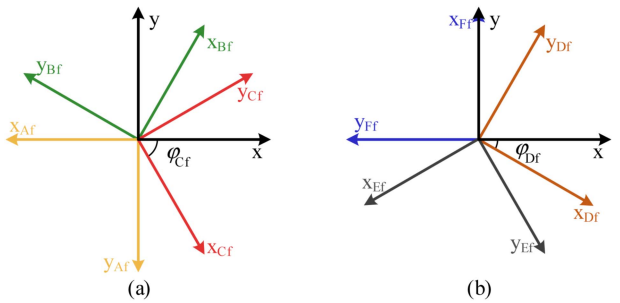

Fig. 3. Faulty phase harmonic space coordinate system. (a) Faulty phase harmonic coordinate system of the first set of windings in the x–y subspace. (b) Faulty phase harmonic coordinate system of the second set of windings in the x–y subspace.

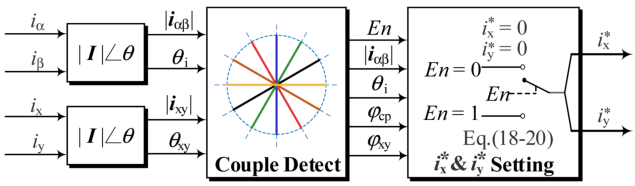

Fig. 4. Natural fault-tolerant control strategy.

axis (the φ_{cp} in Table III), and the positive direction of the y_f-axis lies in the position of x_f-axis counterclockwise 90 electrical degrees.

In the faulty phase coordinate system, the trajectories of the harmonic current vectors in ML and MT modes can be uniformly expressed as

$$\text{ML}: \begin{cases} i_{xf} = |\boldsymbol{i}_{\alpha\beta}| \cos(\theta_f) \\ i_{yf} = 0 \end{cases}$$
$$\text{MT}: \begin{cases} i_{xf} = |\boldsymbol{i}_{\alpha\beta}| \cos(\theta_f) \\ i_{yf} = |\boldsymbol{i}_{\alpha\beta}| \sin(\theta_f) \end{cases} \tag{18}$$

where θ_f is defined as the phase of x–y current vector in the faulty phase harmonic coordinate system

$$\theta_f = \theta_i - \varphi_{cp}. \tag{19}$$

The current components in the x–y subspace coordinate system can be obtained by a simple transformation

$$\begin{bmatrix} i_x \\ i_y \end{bmatrix} = \begin{bmatrix} \cos(\varphi_{xy}) & -\sin(\varphi_{xy}) \\ \sin(\varphi_{xy}) & \cos(\varphi_{xy}) \end{bmatrix} \begin{bmatrix} i_{xf} \\ i_{yf} \end{bmatrix}. \tag{20}$$

The natural fault-tolerant control strategy is shown in Fig. 4. Since there is only leakage inductance in the x–y subspace, the coupling phenomenon between the α-β and x–y subspaces will appear in a short time (several switching period) after the OCF, so the effect of fault transient can be ignored.

It should be noted that mandatory drive derating should be performed under OCF to avoid partial overheating problems. Using I_{lim}^{MT} as the postfault speed loop controller output saturation can ensure the continuity of operation and acceptable performance under fault condition.

C. Implementation of FRML

Previous studies have shown that FRML can be regarded as the result of the joint action of ML mode and MT mode in a certain ratio. And the full TOR natural fault-tolerant control scheme proposed in the previous section provides the possibility for realizing the natural fault-tolerant control and FRML at the same time. Therefore, the key to realize FRML is to determine the optimal ratio combination of ML and MT.

For OCF in phase A, the currents of phase D and E have the maximum amplitude among the remaining healthy phases in FRML strategy. Let us consider phase D as an example, and therefore, its current in the hybrid mode can be expressed as

$$\begin{aligned} i_{D\_FRML} &= A_{ML}\cos(\omega_e t + \varphi_{ML}) + A_{MT}\cos(\omega_e t + \varphi_{MT}) \\ &= A_{D\_FRML}\sin\left(\omega_e t + \frac{\varphi_{ML} + \varphi_{MT}}{2} + \varphi\right) \end{aligned} \tag{21}$$

where φ_{ML} and φ_{MT} can be obtained in Tables I and II, respectively, and A_{ML} and A_{MT} can be expressed as

$$\begin{cases} A_{ML} = \frac{\sqrt{13}(1-k)}{2} |\boldsymbol{i}_{\alpha\beta}| \\ A_{MT} = \sqrt{3}k\, |\boldsymbol{i}_{\alpha\beta}| \end{cases} \tag{22}$$

where k is defined as the ratio of $|\boldsymbol{i}_{\alpha\beta\_MT}| to |\boldsymbol{i}_{\alpha\beta}|$.

The phase-D current amplitude $A_{D\cdot FRML}$ can be specifically expressed as

$$A_{D\_FRML} = \sqrt{A_{ML}^2 + A_{MT}^2 + 2A_{ML}A_{MT}\cos(\varphi_{ML} - \varphi_{MT})}. \tag{23}$$

Considering the constraints of the phase currents under single-phase OCF, $A_{D\cdot FRML}$ needs to meet

$$\sqrt{A_{ML}^2 + A_{MT}^2 + 2A_{ML}A_{MT}\cos(\varphi_{ML} - \varphi_{MT})} \le I_{rt}. \tag{24}$$

Aiming to achieve FRML, a minimum k is required for each torque reference. It is not hard to find that the minimum k can be obtained if and only if the left-hand and right-hand sides of (20) are equal. The expected k can be expressed as

$$k = \frac{|\boldsymbol{i}_{\alpha\beta}| - 2\sqrt{I_{rt}^2 - 3|\boldsymbol{i}_{\alpha\beta}|^2}}{|\boldsymbol{i}_{\alpha\beta}|}. \tag{25}$$

According to (14) and (21), the x–y subspace current references satisfying FRML in the fault phase harmonic space coordinate system under OCF can be expressed as

$$\text{FRML}: \begin{cases} i_{xf} = |\boldsymbol{i}_{\alpha\beta}| \cos(\theta_f) \\ i_{yf} = k\, |\boldsymbol{i}_{\alpha\beta}| \sin(\theta_f). \end{cases} \tag{26}$$

Finally, the x–y subspace current references can be obtained according to (20).

In summary, natural fault-tolerant control of FRML (NFRML) can be achieved without fault diagnosis and localization after single-phase OCFs. A detailed comparison of the proposed NFRML scheme with the existing methods is presented in the next section.

TABLE IV
COMPARISON OF COPPER LOSSES AND TORQUE OUTPUT CAPABILITY

Fault-tolerant strategy	Maximum RMS phase current (p.u.)	Maximum single-phase copper loss (p.u.)	Total copper loss (p.u.)	Torque output capability
Normal operation	1	1	1	100%
ML scheme [13]	1.803	3.25	1.429	55.5%
MT scheme I [13]	1.732	3	2	57.7%
MT scheme II [11]	1.512	2.286	1.588	66.1%
MT scheme III [12]	1.364	1.861	1.524	73.3%
FRML scheme I [16]	1.732–1.803	3~3.25	1.429~2	57.7%
FRML scheme II [18]	1.732–1.803	3~3.25	1.429~2	57.7%
FRML scheme III [20]	1.732–1.803	3~3.25	1.429~2	57.7%
Proposed NFRML scheme	1.732–1.803	3~3.25	1.429~2	57.7%

TABLE V
COMPARISON OF IMPLEMENTATION COMPLEXITY

Fault-tolerant strategy	Computational efforts	Storage cost	Control complexity	Total complexity
ML scheme [13]	+	++	+	++
MT scheme I [13]	+	++	+	++
MT scheme II [11]	++	++	+++	+++
MT scheme III [12]	++	++	+++	+++
FRML scheme I [16]	++	+++	+	+++
FRML scheme II [18]	+++	+	+	+++
FRML scheme III [20]	+	++	+	++
Proposed NFRML scheme	+	+	+	+

"+++", "++", and "+" mean high, medium, and low, respectively.

D. Comparison of Different Strategies

In this section, the copper losses, torque output capability, and implementation effort of different strategies are compared to clarify the improvement of the proposed strategy.

The copper losses and torque output capability of the proposed NFRML scheme are compared with seven existing ML, MT, and FRML strategies, as given in Table IV. The single-phase copper loss can be calculated according to [12]. For ease of comparison, the copper losses are expressed in per unit (p.u.). The copper loss and torque output capability of normal operation are considered as 1 p.u. and 100%, respectively. In general, these strategies can be classified into two categories according to the phase current patterns: sinusoidal phase current pattern and nonsinusoidal phase current pattern. The ML scheme in [13], MT scheme I in [13], FRML schemes I–III in [16], [18], and [20], and the proposed scheme belong to the former, whereas the MT schemes II and III belong to the latter. It can be observed that all the torque output capability of the four FRML schemes is 57.7%, which is the same as the MT scheme I in [13]. Besides, the copper losses of all the four FRML schemes lie between ML and MT with sinusoidal current patterns. By comparison, the MT schemes II and III with nonsinusoidal current patterns can achieve higher torque output capability and lower copper losses simultaneously. The MT scheme II in [11] reduces the total copper losses to 1.588 p.u. and enlarges the torque output capability to 66.1% of normal operation. In MT scheme III [12], the total copper losses and torque output capability are further optimized to 1.524 p.u. and 73.3%, respectively. It should be noted that the remaining healthy phase currents of these schemes show heterogeneous feature. The unbalanced phase currents generate unbalanced phase copper losses. The schemes with nonsinusoidal current patterns shows better phase copper losses performance than that with sinusoidal current patterns thanks to the more thorough current optimization. Furthermore, the response capability of the system under different strategies can be determined according to the torque output capability of the strategy.

Although the performance of copper losses and torque output capability of the fault-tolerant schemes with sinusoidal current patterns are poor than that with nonsinusoidal patterns, the implementation effort of the former is lower than the latter according to Table V. The existing methods need to obtain the optimal current reference by offline or online optimization. Besides, to fulfill the strategies with nonsinusoidal patterns, data-fitting method is usually employed to getting the analytical expressions and high-performance current controllers are required to track the current references. The proposed scheme replaces the tedious optimization process and need not to pre-store extra optimal current references. In addition, the sinusoidal current patterns facilitate the design and tunning process of current controller.

To sum up, the main improvement of the proposed scheme is not for further improving the copper losses and torque output capability performance but for reducing the implementation complexity and improving the integration of the scheme.

IV. EXPERIMENTAL VERIFICATION

The block diagram of the control scheme is shown in Fig. 5(a). DTP-PMSM is controlled by field-oriented control and i_{d} is set as 0. The VSD is adopted to transform the phase currents into α-β and x–y subspaces. PI controller is used as the controller of speed-loop and current-loops in the α-β subspace. Thanks to the certain gain at the resonance frequency, quasi-proportional-resonant (QPR) controller is used to compensate the harmonics caused by the machine/converter asymmetry and regulate the fundamental frequency component of x–y subspace in postfault operation. It should be noted that the x–y current reference is generated by NFRML strategy, which is highlight in Fig. 5(a).

The proposed strategy is validated on the experimental setup shown in Fig. 5(b). The DTP-PMSM is fed by two three-phase two-level inverters with a common dc power. The DTP-PMSM is load coupling its shaft to a three-phase PMSM. The stator of

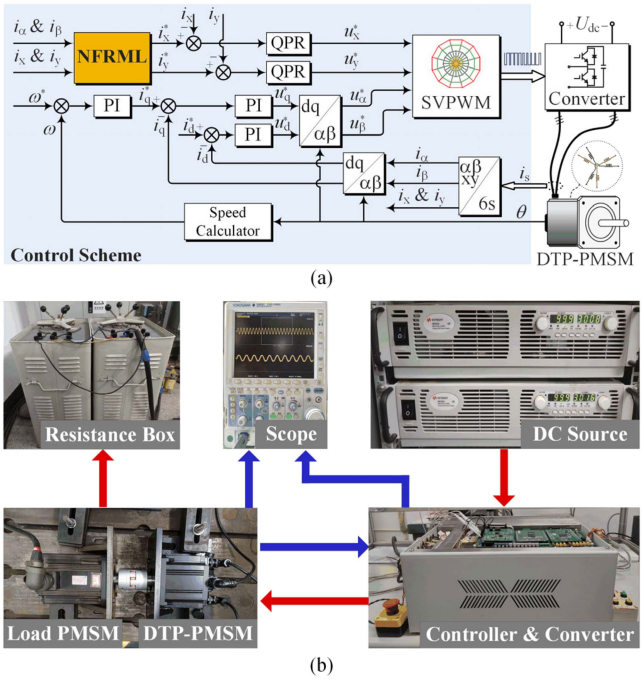

Fig. 5. Control scheme and experimental setup. (a) Block diagram of the NFRML scheme. (b) Experimental setup.

TABLE VI
PARAMETERS OF THE EXPERIMENTAL SETUP

Parameter	Symbol	Value	Unit
Switching frequency	f_s	10	kHz
DC Bus voltage	U_{dc}	400	V
Stator resistance	R	0.6	Ω
d-axis inductance	L_d	13.8	mH
q-axis inductance	L_q	20.6	mH
Permanent magnet flux	Ψ_f	0.218	Wb
Moment of inertia	J	0.005	kg·m^2
Rated current	I_{rt}	3.25	A
Rated speed	n	2000	r/min

the PMSM is connected to a variable resistance load, and the load torque is consequently speed dependent. It should be emphasized that the torque of the tested DTP-PMSM is estimated according to (6). The single-phase OCF have been provoked using a disconnector implemented between the inverter and the machine. Consequently, the current cannot flow anymore in the postfault operation. The control strategy is implemented in a microcontroller TMS320F28379D, and the parameters of the experimental setup are given in Table VI.

A. Transition From Prefault to Postfault Situation

The prefault to postfault performance under different load conditions of the proposed scheme is verified in this section. In addition, the results also show the performance of the x–y subspace controller. In the first condition, the motor is run at 500 r/min with a load of 5 N.m ($|\boldsymbol{i}_{\alpha\beta}| = 1.52\text{A}$) during the entire operation, and the results of transient process are shown in Fig. 6(a). It is visible that the currents are closer to standard sinusoidal waveforms, thanks to the well-tuned PI and QPR controllers. The x–y subspace current components remain almost zero, and the α-β current trace is almost a circular with a radius of 1.5 A. After the OCF in phase A is provoked, the x-axis current, in turn, becomes sinusoidal. According to [13], the proposed scheme works in the ML mode in this fault scenario, the y-axis current follows its zero-reference value. The currents in the remaining healthy phases exhibits good sinusoidal waveforms with different amplitude and the α-β and x–y currents trajectories behave as expected from theory. In the second condition, the motor is run at 500 r/min with a load of 5.9 N.m ($|\boldsymbol{i}_{\alpha\beta}| = 1.82\text{A}$) in prefault and postfault operation. The results of transient processes are shown in Fig. 6(b). In the prefault and postfault operation, nearly the same excellent steady-state performances as first condition are shown. Note that the proposed scheme operates in the hybrid mode according to [13], so that the trajectory of x–y current is no longer a straight line, but an ellipse-like trajectory as expected. In the third condition, the motor in run at 500 r/min with a load of 6.1 N.m ($|\boldsymbol{i}_{\alpha\beta}| = 1.87\text{A}$) in prefault and postfault operations. The results of transient processes are shown in Fig. 6(c). It is worth noting that the proposed scheme operates in the MT mode under this condition, and the α-β and x–y current traces are basically the same circular, which is consistent with the theoretical expectation [13].

To verify the universality of the proposed strategy, the effectiveness of the proposed scheme under different single-phase OCF conditions and higher speed condition is considered. First, phase-E OCF condition is taken as an example. The experiment setting and work conditions are the same as the former. The current and torque control performance in the prefault and postfault operations are the same as the former experiment (see Fig. 7). Comparing the current traces under phase-E OCF and phase-A OCF, it can be seen that the x–y subspace current trace shows different characteristics in these two fault conditions. From another point of view, the same shape characteristic of x–y current trace in the same mode can be observed under different fault conditions. Moreover, with the increase of torque, the trajectories under different fault conditions show the same variation process. The proposed scheme is also evaluated at a higher speed condition. In this experiment, the motor is run at 1500 r/min, and the load torque setting is the same as the previous experiments. The experimental results are shown in Fig. 8 . It can also be seen that although the torque distortion is relatively higher in the higher speed, the x–y current trace has the same characteristic as the traces shown in Fig. 6. It should be noted that although there is a certain torque disturbance during the fault transient, the speed is smooth thanks to the timely intervention of the fault-tolerant control strategy. The above results indicate that there is no phase current exceeding the rated value in the postfault operation, regardless of if the amplitude of the α-β current exceed $\text{I}_{\text{lim}}^{\text{MT}}$.

As a main conclusion of the above experiments, it can be stated that the proposed scheme is universal to different fault scenarios and operating conditions.

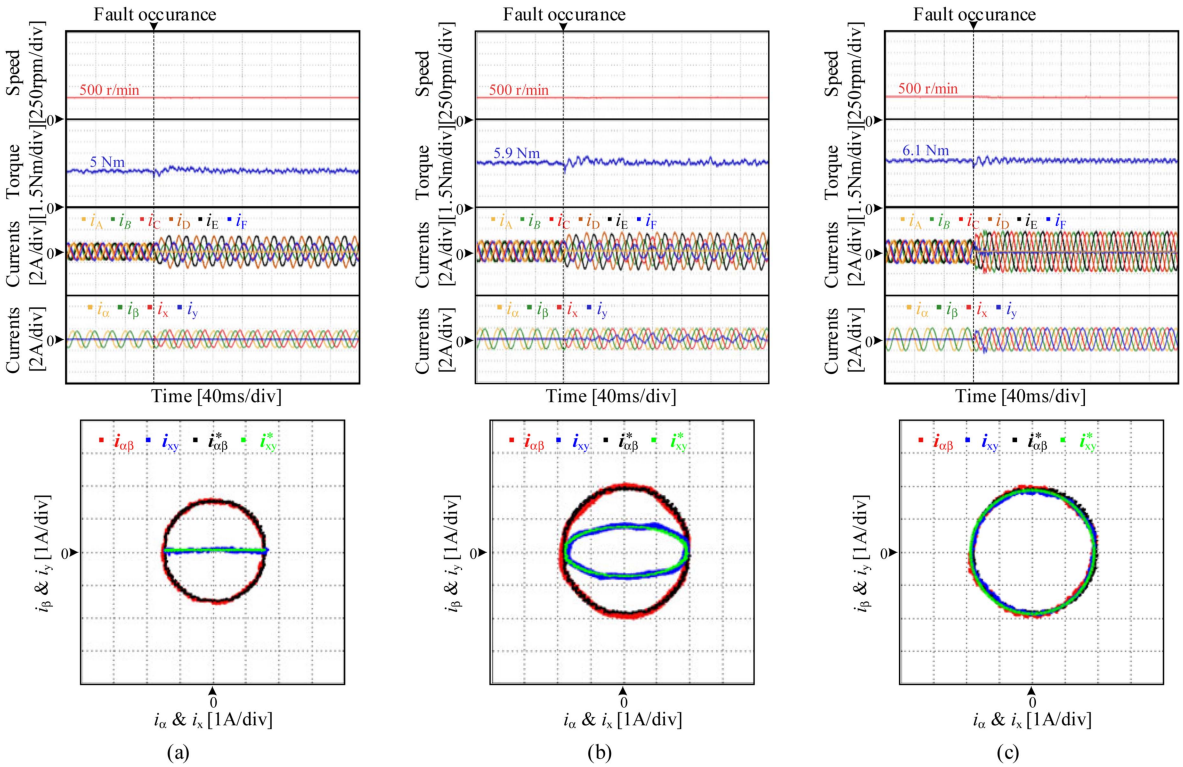

Fig. 6. Transitional experiments from fault-free condition to phase-A opened condition at 500 r/min. From top to bottom: Speed, torque, phase currents, α-β and x–y currents, and current traces in α-β and x–y subspaces during fault-tolerant operation. (a) $|\boldsymbol{i}_{\alpha\beta}| = 0.46I_{\rm rt}$. (b) $|\boldsymbol{i}_{\alpha\beta}| = 0.56I_{\rm rt}$. (c) $|\boldsymbol{i}_{\alpha\beta}| = 0.577I_{\rm rt}$.

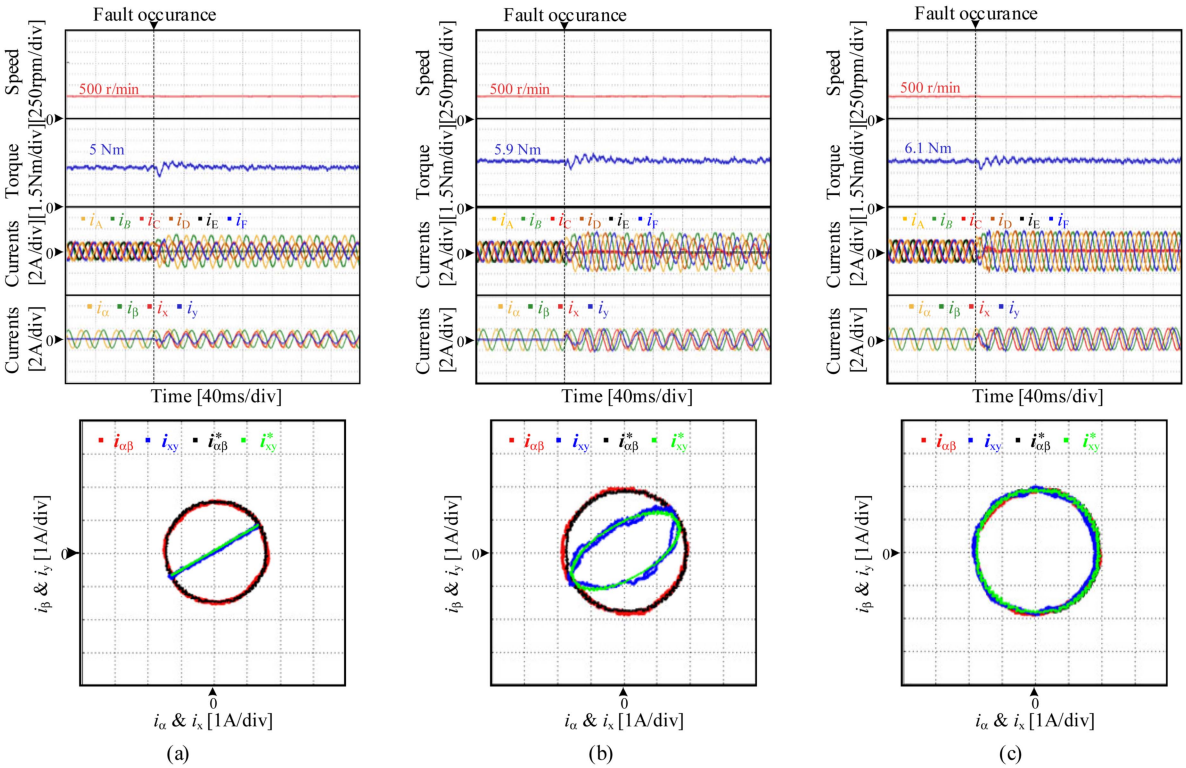

Fig. 7. Transitional experiments from fault-free condition to phase-E opened condition at 500 r/min. From top to bottom: Speed, torque, phase currents, α-β and x–y currents, and current traces in α-β and x–y subspaces during fault-tolerant operation. (a) $|\boldsymbol{i}_{\alpha\beta}| = 0.46I_{\rm rt}$. (b) $|\boldsymbol{i}_{\alpha\beta}| = 0.56I_{\rm rt}$. (c) $|\boldsymbol{i}_{\alpha\beta}| = 0.577I_{\rm rt}$.

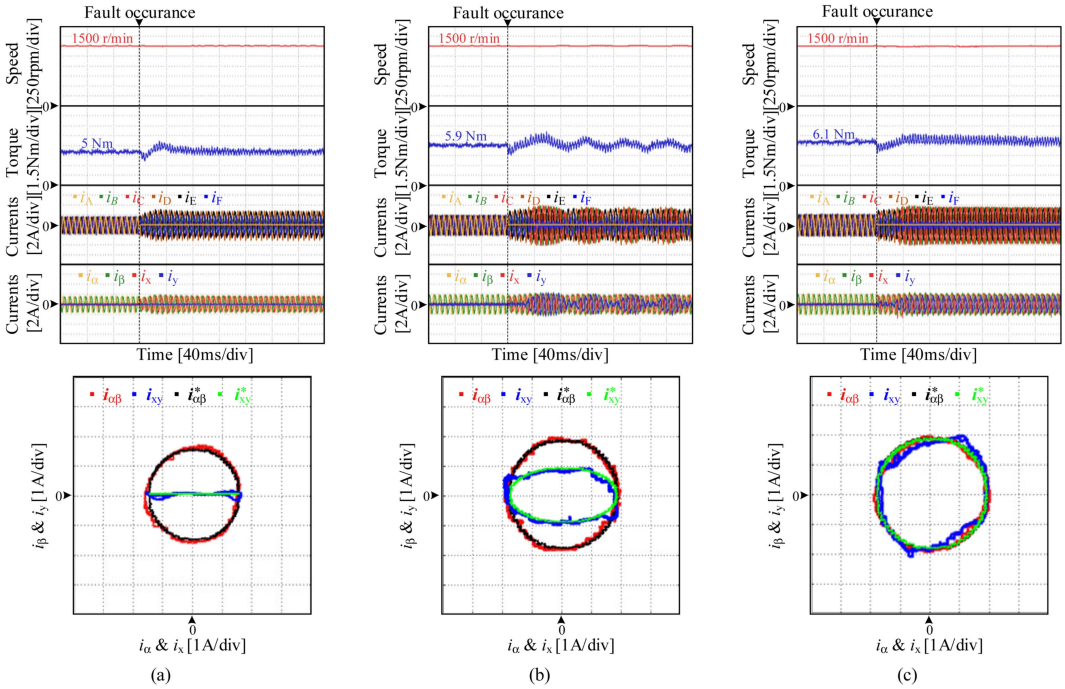

Fig. 8. Transitional experiments from fault-free condition to phase-A opened condition at 1500 r/min. From top to bottom: Speed, torque, phase currents, α-β and x–y currents, and current traces in α-β and x–y subspace during fault-tolerant operation. (a) $|\boldsymbol{i}_{\alpha\beta}| = 0.46I_{\mathrm{rt}}$. (b) $|\boldsymbol{i}_{\alpha\beta}| = 0.56I_{\mathrm{rt}}$. (c) $|\boldsymbol{i}_{\alpha\beta}| = 0.577I_{\mathrm{rt}}$.

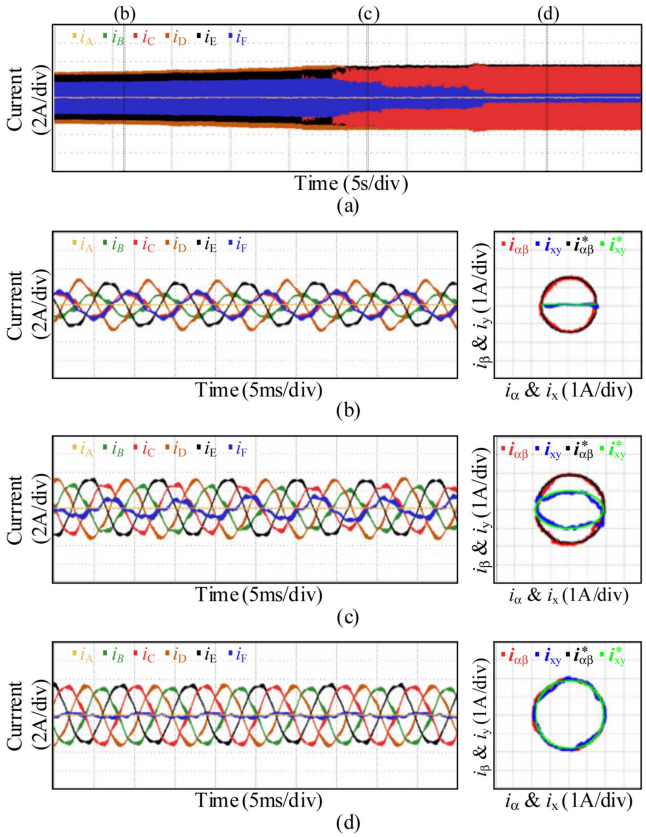

Fig. 9. Phase currents and current traces in α-β and x–y subspaces as load increases under phase-A OCF operation at 1500 r/min. (a) Overall process. (b) $|\boldsymbol{i}_{\alpha\beta}| = 0.46I_{\mathrm{rt}}$. (c) $|\boldsymbol{i}_{\alpha\beta}| = 0.56I_{\mathrm{rt}}$. (d) $|\boldsymbol{i}_{\alpha\beta}| = 0.577I_{\mathrm{rt}}$.

B. Dynamic and Steady-State Performance

In this section, the dynamic performance and steady-state performance of the proposed scheme are verified. To begin with, the dynamic performance is evaluated under load step and speed step conditions in the normal and phase-A OCF conditions, respectively. First, the speed reference is step changed from -500 to 500 r/min and the load torque is maintained at 2 N.m. The speed tracks the reference value within 0.2 s in the normal operation [see Fig. 10(a)], and this process takes about 0.35 s in the postfault operation due to the torque derating. It should be noted that during the speed step process, the proposed scheme operates in MT mode to achieve the MT output [see Fig. 10(b)], which proves the effectiveness of the proposed scheme. Second, the load is step changed from 2 to 5 N.m and back to 2 N.m, and the speed reference is maintained at 500 r/min. It can be seen from Fig. 10(c) and (d) that the torque response ability during the normal and fault-tolerant operations is basically the same, and the speed is stable without obvious fluctuation during postfault operation. Moreover, the x–y currents are not affected by both load step and speed step under normal operation [see Fig. 10(a) and (c)]. According to the results shown in Fig. 10, it can be concluded that the proposed scheme has good dynamic performance and robustness.

In addition to the dynamic performance, torque ripple, total harmonic distortion (THD) of phase currents, and system efficiency under normal and fault-tolerant conditions are evaluated at 500 r/min steady-state operation. The results are summarized in Table VII. In the normal operation, the average torque is about 5 N.m, and the peak-to-peak value of the torque ripple

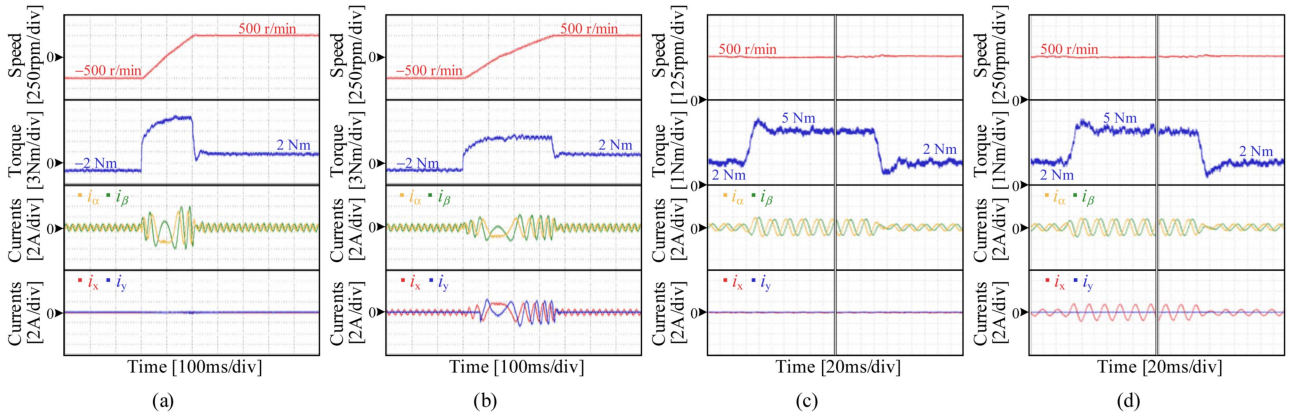

Fig. 10. Load and speed step responses of the NFRML in normal and fault-tolerant operation. From top to bottom: Speed, torque, α-β currents and x–y currents. (a) Speed step response in normal operation. (b) Speed step response under phase-A OCF operation. (c) Load step response in normal operation. (d) Load step response under phase-A OCF operation.

TABLE VII
STEADY-STATE PERFORMANCE UNDER NORMAL AND FAULT-TOLERANT OPERATION

	Torque ripple (%)	THD of current (%)	Efficiency (%)
Normal operation	12.40%	4.81%	95.73%
FTC in the ML mode	20.42%	5.07%	94.61%
FTC in the hybrid mode	21.41%	7.35%	94.17%
FTC in the MT mode	20.63%	6.17%	94.56%

is about 0.62 N.m (12.40% of the average torque). Compared with the normal operation, the torque ripple under fault-tolerant operation is significantly increased (see Table VII), which is mainly due to the OCF. Besides, the THD of phase currents in the ML and MT mode is basically the same as the normal operation condition, whereas the phase currents in the hybrid mode is distorted and the THD of the phase current is slightly higher than that of other conditions. The reason is that the current injected to realize FRML under fault-tolerant operation is affected by the torque ripple. It should be emphasized that the current injected to achieve FRML does not significantly decrease the system efficiency, which can be seen in the fourth column of Table VII.

C. Full TOR Operation Performance

The effectiveness of the proposed scheme in the full TOR is verified in this section. The load of the motor starts with a torque of 1.8 N.m and increase to 6.1 N.m, i.e., the amplitude of α-β current equal to $\mathrm{I}_{\mathrm{lim}}^{\mathrm{MT}}$. The speed reference is maintained at 1500 r/min during this process.

The overall current waveforms of the process is shown in Fig. 9(a), and the phase currents and subspace current vector traces of case $|\boldsymbol{i}_{\alpha\beta}| = 0.46I_{\mathrm{rt}}$, $|\boldsymbol{i}_{\alpha\beta}| = 0.56I_{\mathrm{rt}}$, and $|\boldsymbol{i}_{\alpha\beta}| = 0.577I_{\mathrm{rt}}$ are depicted in Fig. 9(b)–(d), respectively. The proposed scheme experienced a process from the ML mode [see Fig. 9(b)], hybrid mode [see Fig. 9(c)], MT mode [see Fig. 9(d)].

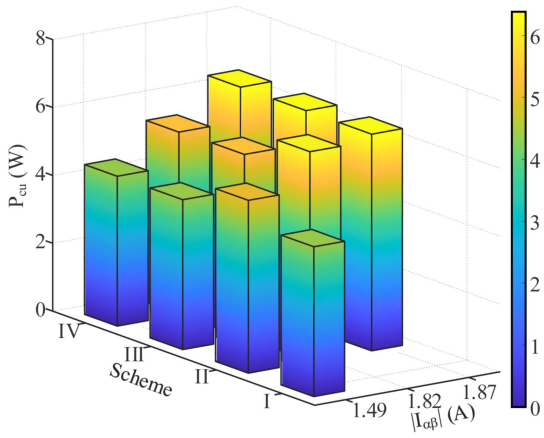

Fig. 11. Comparison of copper loss for different schemes.

The trajectory deviation between x–y subspace current vector and its reference is mainly caused by the current ripple of α-β currents, because theoretical currents range of hybrid mode in the experiment is relatively small (1.80–1.87A). Among these results, phase currents and its trajectories show similar features as expected from theory.

Finally, in order to verify the unity of the proposed algorithm, ML scheme (scheme-I), MT scheme (scheme-II), UCFRML in [18] (scheme-III), and the proposed NFRML scheme in this article (scheme-IV) are also compared in terms of copper loss and torque output capability. The comparison results are shown in Fig. 11. In the ML mode (the case of $|\boldsymbol{i}_{\alpha\beta}| = 0.46I_{\mathrm{rt}}$), schemes I, III, and IV produce almost the same copper loss of 4.41 W, and the scheme II produces the highest copper loss of 5.08 W. In the hybrid mode (the case of $|\boldsymbol{i}_{\alpha\beta}| = 0.56I_{\mathrm{rt}}$), the scheme-I cannot generate required torque under the current constraints, and the copper loss in the scheme-IV (about 5.38 W) is lower than scheme-III (about 5.42 W). Similarly, scheme-II produces the highest copper loss of 6.19 W. In the MT mode, except for scheme-I, the other three strategies generate the same copper loss (about 6.38 W).

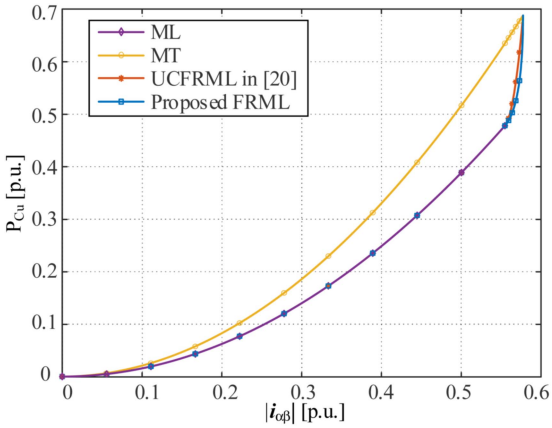

Fig. 12. Comparison of the ML, MT, traditional FRML, and the proposed NFRML strategies for DTP-PMSM.

For a more comprehensive comparison and ease of understanding, the normalized copper losses under different loads are shown in Fig. 12. It can be seen that the proposed scheme has the minimum stator copper loss in the full TOR, which is consistent with the theoretical analysis.

All the above results demonstrate the effectiveness of the proposed natural FRML fault-tolerant control scheme. It can be considered that the proposed scheme, to a great extent, solves the problem presented in the introduction, i.e., achieving high-performance and high efficiency fault-tolerant control effects with a simple fault-tolerant control strategy. In addition, the strategy is designed according to the features of different subspace current vector trajectories of DTP-PMSM, so that it has the potential to be easily extended to other multiphase motors.

V. Conclusion

The existing fault-tolerant control strategies for DTP-PMSM drive OCF cannot achieve FRML and natural fault-tolerant control simultaneously. This article approached this problem, in some degree, by the proposed NFRML strategy. The x–y subspace current references are calculated according to the relation between the α-β and x–y subspace current vector trajectories. Furthermore, FRML is considered as the result of the joint action of ML and MT, and the mathematical expression for calculating the optimal ratio of MT and ML is given. Comparing with existing methods, the proposed strategy has the advantages of low storage cost and easy to implement. Limited by the experimental condition, only the effectiveness of the strategy in DTP-PMSM is verified in this article. However, it is worth noting that the proposed scheme is designed according to the current vector trajectories in VSD model and has the potential to be extended to other types of multiphase motor drives. It should be emphasized that the proposed method is implemented under the restrictions of sinusoidal current patterns, and the torque output capability and copper losses of the drive system can still be further improved. Therefore, further improving the TOR and reducing the copper loss of the system under nonsinusoidal phase current constraints may be a future direction of the FRML strategy.

References

[1] M. J. Duran and F. Barrero, "Recent advances in the design, modeling, and control of multiphase machines—Part II," *IEEE Trans. Ind. Electron.*, vol. 63, no. 1, pp. 459–468, Jan. 2016.

[2] E. Levi, F. Barrero, and M. J. Duran, "Multiphase machines and drives-revisited," *IEEE Trans. Ind. Electron.*, vol. 63, no. 1, pp. 429–432, Jan. 2016.

[3] Z. Zhu, S. Wang, B. Shao, L. Yan, P. Xu, and Y. Ren, "Advances in dual-three-phase permanent magnet synchronous machines and control techniques," *Energies*, vol. 14, no. 22, Nov. 2021, Art. no. 7508.

[4] Z. Liang, D. Liang, P. Kou, and S. Jia, "Postfault control and harmonic current suppression for a symmetrical dual three-phase SPMSM drive under single-phase open-circuit fault," *IEEE Access*, vol. 8, pp. 67674–67686, 2020.

[5] T.-H. Liu, J.-R. Fu, and T. A. Lipo, "A strategy for improving reliability of field-oriented controlled induction motor drives," *IEEE Trans. Ind. Appl.*, vol. 29, no. 5, pp. 910–918, Sep./Oct. 1993.

[6] F.-J. Lin, Y.-C. Hung, and M.-T. Tsai, "Fault-tolerant control for six-phase PMSM drive system via intelligent complementary sliding-mode control using TSKFNN-AMF," *IEEE Trans. Ind. Electron.*, vol. 60, no. 12, pp. 5747–5762, Dec. 2013.

[7] J. Cui, J. Ji, W. Zhao, T. Tao, L. Huang, and H. Tang, "Decoupled fault-tolerant model predictive current control for dual three-phase PMSMs with harmonic compensation," *IEEE Trans. Power Electron.*, vol. 38, no. 2, pp. 2285–2294, Feb. 2023.

[8] Y. Hu, Z. Q. Zhu, and Z. Wu, "Modelling and vector control of dual three-phase PMSM with one-phase open," *Inst. Eng. Technol. Electric Power Appl.*, vol. 15, no. 7, pp. 847–860, Jul. 2021.

[9] X. Wang, Z. Wang, Z. Xu, W. Wang, B. Wang, and Z. Zou, "Deadbeat predictive current control-based fault-tolerant scheme for dual three-phase PMSM drives," *IEEE J. Emerg. Sel. Topics Power Electron.*, vol. 9, no. 2, pp. 1591–1604, Apr. 2021.

[10] X. Wang, Z. Wang, M. He, Q. Zhou, X. Liu, and X. Meng, "Fault-tolerant control of dual three-phase PMSM drives with minimized copper loss," *IEEE Trans. Power Electron.*, vol. 36, no. 11, pp. 12938–12953, Nov. 2021.

[11] W. Wang, J. Zhang, M. Cheng, and S. Li, "Fault-tolerant control of dual three-phase permanent-magnet synchronous machine drives under open-phase faults," *IEEE Trans. Power Electron.*, vol. 32, no. 3, pp. 2052–2063, Mar. 2017.

[12] L. Jin, Y. Mao, X. Wang, P. Shi, L. Lu, and Z. Wang, "Optimization-based maximum-torque fault-tolerant control of dual three-phase PMSM drives under open-phase fault," *IEEE Trans. Power Electron.*, vol. 38, no. 3, pp. 3653–3663, Mar. 2023.

[13] H. S. Che, M. J. Duran, E. Levi, M. Jones, W.-P. Hew, and N. A. Rahim, "Postfault operation of an asymmetrical six-phase induction machine with single and two isolated neutral points," *IEEE Trans. Power Electron.*, vol. 29, no. 10, pp. 5406–5416, Oct. 2014.

[14] D.-K. Son, D.-K. Kang, D.-I. Son, S.-H. Kwon, and G.-H. Lee, "Hybrid mode control of an asymmetric dual three-phase synchronous motor under single-phase open fault," *IEEE Access*, vol. 10, pp. 53250–53264, 2022.

[15] Y. Hu, Y. Feng, and X. Li, "Fault-tolerant hybrid current control of dual three-phase PMSM with one phase open," *IEEE J. Emerg. Sel. Topics Power Electron.*, vol. 10, no. 3, pp. 3418–3426, Jun. 2022.

[16] F. Baneira, J. Doval-Gandoy, A. G. Yepes, O. Lopez, and D. Perez-Estevez, "Control strategy for multiphase drives with minimum losses in the full torque operation range under single open-phase fault," *IEEE Trans. Power Electron.*, vol. 32, no. 8, pp. 6275–6285, Aug. 2017.

[17] A. G. Yepes, J. Doval-Gandoy, F. Baneira, and H. A. Toliyat, "Control strategy for dual three-phase machines with two open phases providing minimum loss in the full torque operation range," *IEEE Trans. Power Electron.*, vol. 33, no. 12, pp. 10044–10050, Dec. 2018.

[18] J. Sun, Z. Liu, Z. Zheng, and Y. Li, "An online global fault-tolerant control strategy for symmetrical multiphase machines with minimum losses in full torque production range," *IEEE Trans. Power Electron.*, vol. 35, no. 3, pp. 2819–2830, Mar. 2020.

[19] A. G. Yepes et al., "Online control strategy for tolerating resistance asymmetry with minimum copper loss in the full torque range for symmetrical six-phase ac drives," *IEEE Trans. Power Electron.*, vol. 38, no. 1, pp. 151–164, Jan. 2023.

[20] G. Yang, H. Hussain, S. Li, J. Zhang, and J. Yang, "A unified fault-tolerant strategy for multiphase machine with minimum losses in full torque operation range based on closed-form expressions," *IEEE Trans. Power Electron.*, vol. 37, no. 10, pp. 12463–12473, Oct. 2022.

[21] I. G. Prieto, M. J. Duran, P. Garcia-Entrambasaguas, and M. Bermudez, "Field-oriented control of multiphase drives with passive fault tolerance," *IEEE Trans. Ind. Electron.*, vol. 67, no. 9, pp. 7228–7238, Sep. 2020.
[22] I. González-Prieto, M. J. Durán, M. Bermúdez, F. Barrero, and C. Martín, "Assessment of virtual-voltage-based model predictive controllers in six-phase drives under open-phase faults," *IEEE J. Emerg. Sel. Topics Power Electron.*, vol. 8, no. 3, pp. 2634–2644, Sep. 2020.
[23] M. J. Durán, I. Gonzalez-Prieto, and A. Gonzalez-Prieto, "Large virtual voltage vectors for direct controllers in six-phase electric drives," *Int. J. Elect. Power Energy Syst.*, vol. 125, Feb. 2021, Art. no. 106425.
[24] G. Yang, H. Hussain, S. Li, X. Zhang, J. Yang, and C. H. T. Lee, "Design and analysis of universal natural fault-tolerant SVPWM strategy with simplified fault diagnosis for multiphase motor drives," *IEEE J. Emerg. Sel. Topics Power Electron.*, vol. 11, no. 4, pp. 4340–4354, Aug. 2023.
[25] K. Yu, Z. Wang, M. Gu, and X. Wang, "Universal control scheme of dual three-phase PMSM drives with single open-phase fault," *IEEE Trans. Power Electron.*, vol. 37, no. 12, pp. 14034–14039, Dec. 2022.
[26] Z. Song, Y. Jia, and C. Liu, "Open-phase fault-tolerant control strategy for dual three-phase permanent magnet synchronous machines without controller reconfiguration and fault detection," *IEEE Trans. Power Electron.*, vol. 38, no. 1, pp. 789–802, Jan. 2023.
[27] X. Wang, Z. Wang, M. Gu, D. Xiao, J. He, and A. Emadi, "Diagnosis-free self-healing scheme for open-circuit faults in dual three-phase PMSM drives," *IEEE Trans. Power Electron.*, vol. 35, no. 11, pp. 12053–12071, Nov. 2020.
[28] P. Shi, X. Wang, X. Meng, M. He, Y. Mao, and Z. Wang, "Adaptive fault-tolerant control for open-circuit faults in dual three-phase PMSM drives," *IEEE Trans. Power Electron.*, vol. 38, no. 3, pp. 3676–3688, Mar. 2023.
[29] Y. Hu, Z. Q. Zhu, and M. Odavic, "Comparison of two-individual current control and vector space decomposition control for dual three-phase PMSM," *IEEE Trans. Ind. Appl.*, vol. 53, no. 5, pp. 4483–4492, Sep./Oct. 2017.
[30] I. González-Prieto, M. J. Duran, and F. J. Barrero, "Fault-tolerant control of six-phase induction motor drives with variable current injection," *IEEE Trans. Power Electron.*, vol. 32, no. 10, pp. 7894–7903, Oct. 2017.

Qiang Geng (Member, IEEE) was born in Tianjin, China, in 1978. He received the B.S. degree in electrical engineering, the M.S. degree in information and communication engineering, and the Ph.D. degree in electrical engineering from Tianjin University, Tianjin, China, in 2000, 2006, and 2012, respectively.

He is currently a Professor in the School of Electrical Engineering, Tiangong University, Tianjin, and also with the National Local Joint Engineering Research Center of Electrical System Design and Manufacturing. His research interests include electrical machines and motor drives, electric drive systems of electric vehicles, power electronics, and control of multimotor system.

Zhongchen Li was born in Henan, China, in 1998. He received the B.S. and M.S. degrees in electrical engineering in 2020 and 2022, respectively, from the Tiangong University, Tianjin, China, where he is currently working toward the Ph.D. degree in electronic information with the School of Electronic and Information Engineering.

His current research interests include fault diagnosis and tolerant control of multiphase and multimotor drive systems.

Huimin Wang (Member, IEEE) received the B.S. and Ph.D. degrees in electrical engineering from Tianjin University, Tianjin, China, in 2005 and 2011 respectively.

She is currently a Professor with the School of Electrical Engineering, Tiangong University, and also with the National Local Joint Engineering Research Center of Electrical Machine System Design and Manufacturing, Tianjin. Her current research focuses on the design, optimization, and control of permanent magnet machine.

Guozheng Zhang (Member, IEEE) was born in Datong, China, in 1985. He received the B.S. degree from Tianjin University, Tianjin, China, in 2008, the M.S. degree from the Tianjin University of Science and Technology, Tianjin, China, in 2011, and the Ph.D. degree from Tianjin University, Tianjin, China, in 2017, all in electrical engineering.

He is currently an Associate Professor with the School of Electrical Engineering, Tiangong University, Tianjin, and also with the National Local Joint Engineering Research Center of Electrical System Design and Manufacturing. His research interests include electrical machines, multilevel converters, and their control systems.

Zhanqing Zhou (Member, IEEE) was born in Ningxia, China, in 1989. He received the B.S. and Ph.D. degrees in electrical engineering from Tianjin University, Tianjin, China, in 2010 and 2017, respectively.

He is currently an Associate Professor with the School of Electrical Engineering, Tiangong University, Tianjin, and also with the National Local Joint Engineering Research Center of Electrical System Design and Manufacturing. His research interests include electrical machines and their control systems, power electronics, and renewable energy systems.